MODEL ADJUSTED MATCHED FILTER FOR METHANE PLUME DETECTION ON PRISMA HYPERSPECTRAL IMAGES

E. Ouerghi, T. Ehret, Gabriele Facciolo, E. Meinhardt, C. de Franchis, A. Groshenry, J.-M. Morel

MODEL ADJUSTED MATCHED FILTER FOR METHANE PLUME DETECTION ON PRISMA HYPERSPECTRAL IMAGES

E. Ouerghi, T. Ehret
G. Facciolo, E. Meinhardt

Université Paris-Saclay, CNRS
ENS Paris-Saclay, Centre Borelli

C. de Franchis
A. Groshenry

Kayrros SAS

J.-M. Morel

City University of Hong Kong

ABSTRACT

Reducing methane emissions is essential to tackle climate change. Here, we address the problem of detecting automatically point source methane leaks using high resolution hyperspectral images from the PRISMA satellite. We propose an improvement of the classical matched filter method by using an adjustment coefficient. We introduce this new method under the name: Model Adjusted Matched Filter (MAMF). We show that the MAMF method reduces the fraction of false detections compared to the Matched Filter (MF) and the Adaptive Cosine Estimator (ACE) without preventing the detection of plumes. To validate the method, we use a dataset of manually annotated plumes on PRISMA images. We then show that our method outperforms the matched filter and the adaptive cosine estimator in terms of F1 score.

***Index Terms*—** Hyperspectral images, Mahalanobis distance, Prisma, Methane, Anomaly detection

1. INTRODUCTION

In order to detect greenhouse gas fossil fuel emissions from human activities, several satellites have been placed in orbit around the Earth over the past ten years. Here, we focus on PRISMA [1] (PRecursore IperSpettrale della Missione Applicativa), a satellite of the new generation of hyperspectral imagers launched in 2019 by the Italian Space Agency. PRISMA provides hyperspectral images with a high spatial resolution (30m) and a swath of 30 km. Each pixel contains a spectrum with 237 channels between 400nm and 2500nm. We will exploit the two absorption bands of methane present in this wavelength range: the first around 1700nm and the second around 2300nm.

Several methods for the detection of point source methane emissions on PRISMA already exist. One of the most popular approach for this task is the matched filter algorithm [2]. Here we propose an improvement of the matched filter we call Model Adjusted Matched Filter. Our method improves the matched filter by adding an adjustment coefficient. The adjustment coefficient aims at reducing the number of false positives compared to what can be observed with the matched filter or the adaptive cosine estimator.

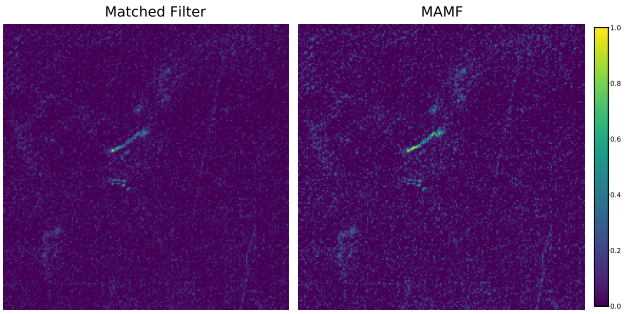

Fig. 1. Comparison between the MF on the left and the MAMF on the right. The MF and MAMF are computed over the same PRISMA image taken in Algeria (08/31/2020).

To validate the method, we evaluate our approach on manually-annotated plumes detected in PRISMA satellite images. We also compare our results to the matched filter [2], which is one of the most popular approach for methane plume detection on PRISMA. We then show that our method outperforms the matched filter and the adaptive cosine estimator [3] based on a comparison of the F1 score.

2. RELATED WORK

In the recent years, multiple approaches have been developed to detect and to quantify methane plumes in satellite images: the inversion of detailed atmospheric absorption models, hyperspectral detection algorithms with in particular the matched filter and finally deep learning for plume segmentation.

Regarding hyperspectral imagers, our main focus here, two main techniques have been applied to detect methane plumes, both aiming at the quantification of the methane concentrations in the observed area.

The first is the iterative maximum a posteriori applied to differential optical absorption spectroscopy (IMAP-DOAS) [4].

This method consists in inverting a complete atmospheric absorption model with an optimal estimation algorithm. It is already used to quantify methane with many hyperspectral instruments [5, 6]. IMAP-DOAS works with sensors that have very different spectral and spatial resolutions, such as AVIRIS [7] and TROPOMI [6]. In the case of TROPOMI, the implementation is based on the work presented in [8] and [9]. The modeling is extremely precise: the atmosphere is divided into several layers to take into account the variations in pressure and temperature that modify the gas absorption coefficients. This model considers not only the absorption of gases but also the absorption and diffusion of aerosols [10] (solid or liquid particles in a gaseous medium) and the back-scattering of the atmosphere.

The second technique is the matched filter [11, 2]. The matched filter is a linear filter that quantifies the presence of an anomaly whose spectral signature is known. The matched filter allows to compute the excess methane concentration with more computational efficiency than the IMAP-DOAS method. However, it only retrieves the concentration of methane whereas the IMAP-DOAS retrieves the concentration of all gases. Several matched filter variations exist [3]. One used for methane plume detection is the Cluster-Tuned Matched Filter (CTMF) [12]. The idea proposed by [12] is to use a modified version of a k-means clustering prior to the matched filter. Spatial clustering allows to obtain results over very large areas without the risk of confusing anomalies due to CH_4 with those due to other gases.

A more recent category of methods for methane plume detection comes from deep learning techniques. The use of deep learning generally involves plume simulation to compensate for the small number of detected plumes in current datasets. For the moment, these methods are only applied to hyperspectral sensors such as PRISMA [13, 14] and TROPOMI [15]. But it is reasonable to expect that in the future these methods will be applied to other hyperspectral sensors. Indeed, recent hyperspectral imagers such as EnMap [16] or EMIT [17] have characteristics which are very close to those of PRISMA. The methods developed on PRISMA can therefore also be applied to these imagers.

3. MATERIALS

We use the level 1 images from the PRISMA satellite. Those images are hyperspectral images with a 30m spatial resolution and contain a spectrum for each pixel with 237 channels between 400nm and 2500nm. Here we are interested in the SWIR region of the spectrum containing 171 channels with a spectral interval of $920 - 2505$nm. Because we are interested here in the detection of methane plumes, we only use channels where methane actually absorbs radiation, i.e. at the peaks of the absorption spectrum. In practice, we use the channels in the $1550 - 1800$nm and $2100 - 2480$nm regions of the spectrum. In the SWIR spectrum, the spectral resolution varies between 9nm and 15nm.

We also use a detailed CH_4 absorption spectrum taken from the HITRAN spectral database [18]. The CH_4 spectrum varies depending on pressure and temperature. However, here we are only interested in the CH_4 spectrum within the bottom layers of the atmosphere (below 1,500 meters above ground). This is because we want to detect CH_4 shortly after being emitted, before it rises and dilutes. Spectrum variations are small in the near-surface atmospheric layers so we selected the CH_4 spectrum at $15°$C and 1 atm to represent near-surface atmospheric conditions.

4. METHOD

4.1. Matched Filter and Mahalanobis distance

One of the most popular methods for detecting methane plumes in hyperspectral images is the matched filter [2]. The matched filter is derived by linearizing an absorption model and then calculating a likelihood ratio between the distribution of a pixel belonging to a plume and the distribution of the background.

Let x be a background observation that follows a multivariate normal distribution with mean μ and covariance matrix Σ. If x_{plume} is an observation in a methane plume, then according to Beer's law we can write

$$x_{plume} = \exp(-\alpha K_{\text{CH4}})x, \tag{1}$$

where α is proportional to the methane density variation in the plume and K_{CH_4} is the diagonal matrix whose coefficients are the ones of the methane absorption spectrum. With these notations, the matched filter detector $\mathcal{D}_{MF}$ is then defined as

$$\mathcal{D}_{MF}(x) = \frac{\mathbf{t}^T\Sigma^{-1}(x-\mu)}{\mathbf{t}^T\Sigma^{-1}\mathbf{t}}, \tag{2}$$

where $\mathbf{t}$ is the target vector is defined by [11, 2] as

$$\mathbf{t} = -K_{\text{CH}_4}\mu. \tag{3}$$

The parameters μ and Σ are computed with their empirical estimates. To take into account the different radiometric responses of the detector elements of the PRISMA sensor, the parameters need to be computed across-track [2]. This means that a different set of parameters is computed for each line of a PRISMA image. This helps to eliminate horizontal artifacts that often appear due to hyperspectral striping [2, 19].

The main drawback of the matched filter is its high false positive rate. The matched filter can detect anomalies that are not in the direction of the target vector if there are outliers. For example, an observation with a high norm leads to a high value for the matched filter. False positives also happen for regions with a very low albedo, such as buildings, roads or water bodies. To avoid false positives, one can use the Adaptive Cosine Estimator (ACE)[3]. The ACE does not depend

on the norm of x but only on the angle between the observation and the target, therefore it will penalize the score of these outliers. The ACE is defined by

$$\mathcal{D}_{ACE}(x) = \frac{\mathcal{D}_{MF}(x)}{\mathcal{M}_D(x)}, \tag{4}$$

where $\mathcal{M}_D$ is the Mahalanobis distance:

$$\mathcal{M}_D(x) = \sqrt{(x-\mu)^T \Sigma^{-1}(x-\mu)}. \tag{5}$$

The Mahalanobis distance represents the distance between the observation and the background distribution.

4.2. The Model Adjusted Matched Filter

While the ACE detector can help with false positives, it still has a main drawback: observations in a plume can have a high Mahalanobis distance which leads to a low value for $\mathcal{D}_{ACE}$. Indeed, observations inside a plume are outliers with respect to the background distribution. Therefore, the use of $\mathcal{M}_D(x)$ in $\mathcal{D}_{ACE}(x)$ can prevent the detection of plumes.

To solve this issue we introduce a model adjustment coefficient to replace $\mathcal{M}_D(x)$. We define it as

$$\begin{aligned}\mathcal{D}_{MA}(x) &= \mathcal{M}_D(x - \mathcal{D}_{MF}(x)\mathbf{t})^2 \\ &= (x - \mu - \mathcal{D}_{MF}(x)\mathbf{t})^T \Sigma^{-1}(x - \mu - \mathcal{D}_{MF}(x)\mathbf{t}).\end{aligned} \tag{6}$$

With $\mathcal{D}_{MA}(x)$, for each observation x we remove the estimated methane excess $\mathcal{D}_{MF}(x)$. Thus, plume pixels will not be outliers when computing the Mahalanobis distance between the corrected observation and the background distribution. In the case of outliers, their anomaly does not perfectly align with the target vector. Therefore, even when compensated by the estimated methane excess those observations will remain outliers and have a high Mahalanobis distance.

We then use $\mathcal{D}_{MA}(x)$ to replace $\mathcal{M}_D(x)$. We call this new detector the Model Adjusted Matched Filter (MAMF)

$$\mathcal{D}_{MAMF}(x) = \frac{\mathcal{D}_{MF}(x)}{\mathcal{D}_{MA}(x)^q}. \tag{7}$$

The exponent q controls the strength of the adjustment. We used simulations to determine the value of q and the detection threshold. Plumes were simulated on PRISMA images using a radiative transfer model and the HITRAN database [18]. In the following, we use the estimated optimal value $q = 0.66$.

5. EXPERIMENTS AND RESULTS

In Figure 1 we can compare the results of the MF and MAMF. In both images we can clearly see the plume which stands out in the center. With the MF the background has lower values than with the MAMF where the background seems to have more noise. However, in both cases, the background values are too low to prevent the detection. Moreover, with the MAMF, the part of the plume with a high contrast is larger than in the MF image. Therefore, performing the detection with the MAMF will allow to detect a larger part of the plume.

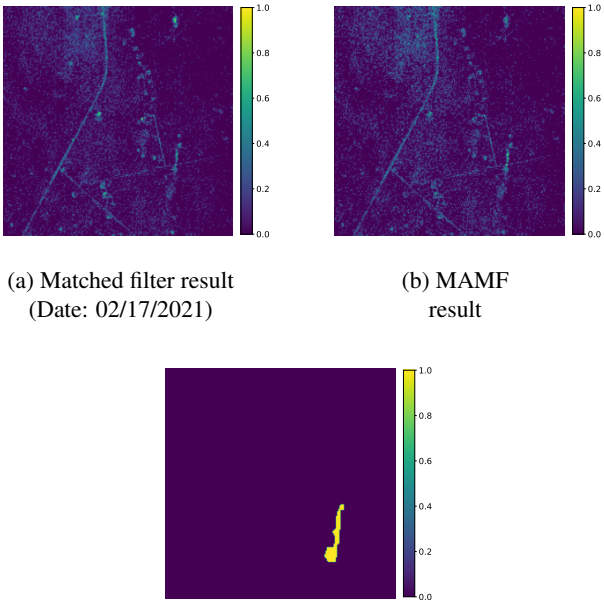

(a) Matched filter result (Date: 02/17/2021)

(b) MAMF result

(c) Ground truth

Fig. 2. Comparison between the Matched Filter and the Model Adjusted Matched Filter (MAMF). The tested methane plume is in the USA.

The example presented in Figure 2 presents more challenges for the detection as we can observe lots of potential false positives in the MF image. Most of them are roads and buildings. They are still visible in the MAMF image but with a way lower contrast. For example, the false positive on the top right corner has higher values than most of the plume pixels in the MF image but this is no longer the case in the MAMF image. In the same way there are two bright false positives around the middle of the MF image but they are nearly blended in the background in the MAMF image. The plume contrast with respect to the background is also higher with the MAMF than with the MF. Therefore, for this image we need to use the MAMF to perform the plume detection without false positives.

Another way to compare the matched filter and the MAMF is to look at the distribution of plume and non-plume pixels along the axis defined by $\mathcal{D}_{MF}$ and $\mathcal{D}_{MA}$. We can observe this distribution in Figure 3. Using the matched filter means that we would have to separate the plume and non-plume distributions using only the vertical axis in Figure 3. However, lots of non-plume pixels have value comparable with plume pixels. The improvement brought by our model adjustment coefficient $\mathcal{D}_{MA}$ is that a significant proportion of non-plume pixels with high $\mathcal{D}_{MF}(x)$ values also have a high $\mathcal{D}_{MA}(x)$ score. This fact makes it easier to separate the two

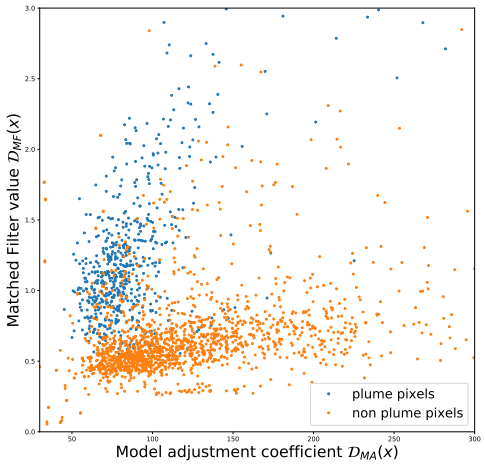

Fig. 3. Scatter plot comparing the distribution of plume and non plume pixels with respect to their matched filter and model adjustment scores.

distributions by looking at the data in the two dimensional space, which means using the MAMF.

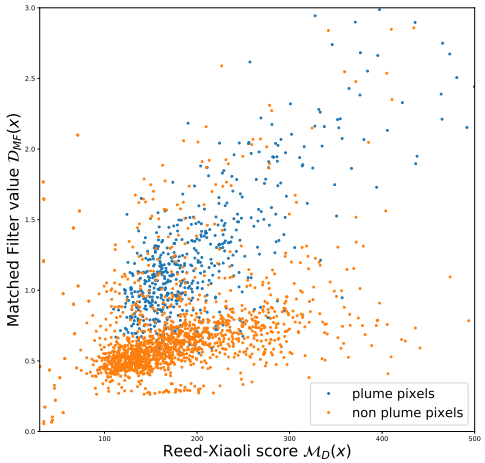

Fig. 4. Scatter plot comparing the distribution of plume and non plume pixels with respect to their matched filter scores and Mahalanobis distances.

In Figure 4, we can observe the same data as in Figure 3 but with $\mathcal{M}_D(x)$ for the horizontal axis instead of $\mathcal{D}_{MA}(x)$. Figure 4 is the visual representation corresponding to the use of ACE. We can observe that unlike Figure 3, a large part of plume pixels have high $\mathcal{M}_D(x)$ scores. Moreover, lots of non-plume pixels have higher $\mathcal{D}_{MF}(x)$ scores and lower $\mathcal{M}_D(x)$ scores than plume pixels. This makes it hard to separate the two distributions in Figure 4. This explains why we expect worse results with ACE than with the MAMF.

The improvements brought by the MAMF can be seen numerically by looking at Table 1. All methods were tested with automatic detection without manual correction. The ground truth images have been manually labeled. In particular, the dataset used here includes the images of the dataset proposed by [13]. Detection thresholds were calculated to maximize the F1 score. In Table 1, we can observe that the MF and ACE give very similar results. The ACE has a higher precision than the MF but this is counterbalanced by the higher recall of the MF. Our method, the MAMF, outperforms both the MF and ACE in recall and in precision. The most significant gain brought by our method is the gain in precision. This could be expected because the idea behind the model adjustment was to reduce the number of false positives.

	Recall	Precision	F1
MF [2]	0.27	0.32	0.29
ACE [3]	0.24	0.37	0.29
MAMF (ours)	**0.39**	**0.56**	**0.46**

Table 1. Detection result of the different methods on our PRISMA plume dataset. Our dataset contains 80 plumes. The detection metrics are computed per plume.

6. CONCLUSION

We have introduced the MAMF, a methane plume detection method based on a variant of the matched filter. It outperforms pre-existing methods both in terms of recall and precision. While the algorithm presented here has been tested on PRISMA satellite images, since the characteristics of PRISMA are very close to those of other hyperspectral instruments such as EnMap or EMIT, it should be possible to extend the use of the MAMF to these instruments as well.

7. REFERENCES

[1] Sergio Cogliati et al., "The prisma imaging spectroscopy mission: overview and first performance analysis," *Remote Sensing of Environment*, vol. 262, pp. 112499, 09 2021.

[2] Luis Guanter, Itziar Irakulis-Loitxate, Javier Gorroño, Elena Sánchez-García, Daniel H. Cusworth, Daniel J. Varon, Sergio Cogliati, and Roberto Colombo, "Mapping methane point emissions with the prisma spaceborne imaging spectrometer," *Remote Sensing of Environment*, vol. 265, pp. 112671, 2021.

[3] James Theiler, "Absorptive weak plume detection on gaussian and non-gaussian background clutter," *IEEE Journal of Selected Topics in Applied Earth Observations and Remote Sensing*, vol. 14, pp. 6842–6854, 2021.

[4] Clive D. Rodgers, "Retrieval of atmospheric temperature and composition from remote measurements of

thermal radiation," *Reviews of Geophysics*, vol. 14, pp. 609–624, 1976.

[5] Christian Frankenberg, Ulrich Platt, and T. Wagner, "Iterative maximum a posteriori (imap)-doas for retrieval of strongly absorbing trace gases: Model studies for ch_4 and co_2 retrieval from near infrared spectra of sciamachy onboard envisat," *Atmospheric Chemistry and Physics*, vol. 5, no. 1, pp. 9–22, 2005.

[6] Sudhanshu Pandey et al., "Satellite observations reveal extreme methane leakage from a natural gas well blowout," *PNAS*, vol. 116, no. 52, pp. 26376–26381, Dec. 2019.

[7] Andrew Thorpe, Christian Frankenberg, and Dar Roberts, "Retrieval techniques for airborne imaging of methane concentrations using high spatial and moderate spectral resolution: application to aviris," *Atmospheric Measurement Techniques Discussions*, vol. 6, 09 2013.

[8] André Butz, Andre Galli, Otto Hasekamp, Jochen Landgraf, Paul Tol, and Ilse Aben, "Tropomi aboard sentinel-5 precursor: Prospective performance of ch4 retrievals for aerosol and cirrus loaded atmospheres," *Remote Sensing of Environment*, vol. 120, no. SI, pp. 267–276, 2012.

[9] Jochen Landgraf, Joost Brugh, Remco Scheepmaker, Tobias Borsdorff, Haili Hu, Sander Houweling, André Butz, Ilse Aben, and Otto Hasekamp, "Carbon monoxide total column retrievals from tropomi shortwave infrared measurements," *Atmospheric Measurement Techniques*, vol. 9, pp. 4955–4975, 10 2016.

[10] André Butz, Otto Hasekamp, Christian Frankenberg, and Ilse. Aben, "Retrievals of atmospheric co2 from simulated space-borne measurements of backscattered near-infrared sunlight: accounting for aerosol effects," *Applied optics*, vol. 48, pp. 3322–36, 07 2009.

[11] James Theiler and Brendt Wohlberg, "Detection of unknown gas-phase chemical plumes in hyperspectral imagery," in *Algorithms and Technologies for Multispectral, Hyperspectral, and Ultraspectral Imagery XIX*, Sylvia S. Shen and Paul E. Lewis, Eds., May 2013, vol. 8743 of *Society of Photo-Optical Instrumentation Engineers (SPIE) Conference Series*, p. 874315.

[12] C.C. Funk, James Theiler, Dar Roberts, and Christoph Borel, "Clustering to improve matched filter detection of weak gas plumes in hyperspectral thermal imagery," *Geoscience and Remote Sensing, IEEE Transactions on*, vol. 39, pp. 1410 – 1420, 08 2001.

[13] Alexis Groshenry, Clement Giron, Thomas Lauvaux, Alexandre d'Aspremont, and Thibaud Ehret, "Detecting methane plumes using prisma: Deep learning model and data augmentation," 2022.

[14] Peter Joyce, Cristina Villena, Yahui Huang, Alex Webb, Manuel Gloor, Fabien Wagner, Martyn Chipperfield, Rocío Barrio Guilló, Christopher Wilson, and Hartmut Boesch, "Using a deep neural network to detect methane point sources and quantify emissions from prisma hyperspectral satellite images," *EGUsphere*, vol. 2022, pp. 1–22, 2022.

[15] Berend Schuit, Joannes Maasakkers, Pieter Bijl, Gourav Mahapatra, Anne-Wil Berg, Sudhanshu Pandey, Alba Lorente, Tobias Borsdorff, Sander Houweling, Daniel Varon, Jason McKeever, Dylan Jervis, Marianne Girard, Itziar Irakulis-Loitxate, Javier Gorroño, Luis Guanter, Daniel Cusworth, and I. Aben, "Automated detection and monitoring of methane super-emitters using satellite data," *Atmospheric Chemistry and Physics Discussions*, vol. 2023, pp. 1–47, 2023.

[16] Guanter et al., "The enmap spaceborne imaging spectroscopy mission for earth observation," *Remote Sensing*, vol. 7, no. 7, pp. 8830–8857, 2015.

[17] Christine L. Bradley, Erik Thingvold, Lori B. Moore, Justin M. Haag, Nasrat A. Raouf, Pantazis Mouroulis, and Robert O. Green, "Optical design of the Earth Surface Mineral Dust Source Investigation (EMIT) imaging spectrometer," in *Imaging Spectrometry XXIV: Applications, Sensors, and Processing*, Emmett J. Ientilucci and Pantazis Mouroulis, Eds. International Society for Optics and Photonics, 2020, vol. 11504, p. 1150402, SPIE.

[18] Iouli E. Gordon, L. S. Rothman, Christian Hill, R. V. Kochanov, Y. Tan, et al., "The HITRAN2016 molecular spectroscopic database," *J Quant Spectrosc Ra*, vol. 203, pp. 3 – 69, Dec. 2017.

[19] P. Tripathi and R. D. Garg, "Feature extraction of desis and prisma hyperspectral remote sensing datasets for geological applications," *The International Archives of the Photogrammetry, Remote Sensing and Spatial Information Sciences*, vol. XLIV-M-3-2021, pp. 169–173, 2021.